possible for nonrotationally symmetric systems, allowing practical designs to be simulated with high accuracy; (2) mechanical fabrication tolerances have advanced materially in the past 15 years; (3) high stability electronic components have become available in the past 10 years, allowing the packaging of many, very high stability, computer-controlled power supplies in a small space; and (4) high-speed small computers are now available for real-time processing of the shadow map Rochigram data to obtain aberration parameters.

We believe aberration correction technology combined with the inherent power of the STEM instrument opens the way for lower voltage, smaller, 'smarter', more easily managed instruments that will be capable of routinely imaging and analysing materials at sub-ångstrom resolution, using several different crystal orientations. Specialized instruments, perhaps using some submillimetre-sized electrostatic imaging elements, may reach the diffraction limit for the imaging electrons. Multiple corrector systems will allow aberration control of both probe size and detector field of view, in a manner somewhat similar to confocal light microscopy. Finally, detailed control of the amplitude and phase of the incident and scattered electron wavefunction will be possible, allowing specific specimen inelastic transitions to be accessed[20]. Thus aberration correction marks a shift towards precise optical control that will allow routine atomic level characterization of defects and interfaces within bulk materials. □

Received 5 April; accepted 4 July 2002; doi:10.1038/nature00972.

1. Scherzer, O. The theoretical resolution limit of the electron microscope. *J. Appl. Phys.* **20,** 20–29 (1949).
2. Haider, M., Uhlemann, S., Schwan, E., Kabius, B. & Urban, K. Electron microscopy image enhanced. *Nature* **392,** 768–769 (1998).
3. Crewe, A. V., Isaacson, M. & Johnson, D. A simple scanning electron microscope. *Rev. Sci. Instrum.* **40,** 241–246 (1969).
4. Voyles, P. M., Muller, D. A., Grazul, J. L., Citrin, P. H. & Gossmann, H.-J. L. Atomic-scale imaging of individual dopant atoms and clusters in highly n-doped bulk Si. *Nature* **416,** 826–829 (2002).
5. Crewe, A. V., Wall, J. & Langmore, J. Visibility of a single atom. *Science* **168,** 1338–1340 (1970).
6. Pennycook, S. J. & Boatner, L. A. Chemically sensitive structure-imaging with a scanning transmission electron microscope. *Nature* **336,** 565–567 (1988).
7. Xu, P., Kirkland, E. J., Silcox, J. & Keyse, R. High resolution imaging of silicon (111) using a 100 KeV STEM. *Ultramicroscopy* **32,** 93–102 (1990).
8. Crewe, A. V., Isaacson, M. & Johnson, D. A high resolution electron spectrometer for use in transmission scanning microscopy. *Rev. Sci. Instrum.* **42,** 411–420 (1971).
9. Batson, P. E. Simultaneous STEM imaging and electron-energy-loss-spectroscopy with atomic-column sensitivity. *Nature* **366,** 727–728 (1993).
10. Muller, D. A., Tzou, Y., Raj, R. & Silcox, J. High resolution EELS at grain boundaries. *Nature* **366,** 725–727 (1993).
11. Browning, N. D., Chisholm, M. F. & Pennycook, S. J. Atomic resolution analysis using a scanning transmission electron microscope. *Nature* **366,** 143–146 (1993).
12. Dellby, N., Krivanek, O. L., Nellist, P. D., Batson, P. E. & Lupini, A. R. Progress in aberration-corrected scanning transmission electron microscopy. *J. Electron. Microsc.* **50,** 177–185 (2001).
13. Batson, P. E. Structural and electronic characterization of a dissociated 60° dislocation in GeSi. *Phys. Rev. B* **61,** 16633–16641 (2000).
14. Ronchi, V. Forty years of history of a grating interferometer. *Appl. Opt.* **3,** 437–450 (1964).
15. Zhang, Z. Y. & Lagally, M. G. Atomistic processes in the early stages of thin film growth. *Science* **276,** 377–383 (1997).
16. Kirkland, E. J. *Advanced Computing in Electron Microscopy* (Plenum, New York, 1998).
17. Kawasaki, T. *et al.* Development of a 1 MV field emission transmission electron microscope. *J. Electron. Microsc.* **49,** 711–718 (2000).
18. O'Keeffe, M. A. *et al.* Sub-ångstrom high resolution transmission electron microscopy at 300 keV. *Ultramicroscopy* **89,** 215–241 (2001).
19. Zuo, J., Kim, Y., O'Keeffe, M. & Spence, J. C. H. Direct observation of d holes and Cu-Cu bonding in Cu_2O. *Nature* **401,** 49–56 (1999).
20. Batson, P. E. Symmetry selected electron energy loss scattering in diamond. *Phys. Rev. Lett.* **70,** 1822–1825 (1993).

Acknowledgements

O.L.K. and N.D. acknowledge partial support for this project from the IBM Corporation.

Competing interests statement

The authors declare that they have no competing financial interests.

Correspondence and requests for materials should be addressed to P.E.B. (e-mail: batson@us.ibm.com).

Experimental evidence for sub-3-fs charge transfer from an aromatic adsorbate to a semiconductor

Joachim Schnadt*, Paul A. Brühwiler*, Luc Patthey†, James N. O'Shea*, Sven Södergren*, Michael Odelius‡, Rajeev Ahuja*, Olof Karis*, Margit Bässler§, Petter Persson*, Hans Siegbahn*, S. Lunell* & Nils Mårtensson§*

* *Department of Physics, Uppsala University, Box 530;* ‡ *Department of Physical Chemistry, Uppsala University, Box 532, 75121 Uppsala, Sweden*
† *Swiss Light Source, Paul-Scherrer-Institut, 5232 Villigen-PSI, Switzerland*
§ *MAX-Lab, University of Lund, Box 118, 22100 Lund, Sweden*

The ultrafast timescale of electron transfer processes is crucial to their role in many biological systems and technological devices. In dye-sensitized solar cells[1–4], the electron transfer from photo-excited dye molecules to nanostructured semiconductor substrates needs to be sufficiently fast to compete effectively against loss processes and thus achieve high solar energy conversion efficiencies[4]. Time-resolved laser techniques indicate an upper limit of 20 to 100 femtoseconds[5–9] for the time needed to inject an electron from a dye into a semiconductor, which corresponds to the timescale on which competing processes such as charge redistribution[10,11] and intramolecular thermalization of excited states[12–14] occur. Here we use resonant photoemission spectroscopy, which has previously been used to monitor electron transfer in simple systems with an order-of-magnitude improvement in time resolution[15,16], to show that electron transfer from an aromatic adsorbate to a TiO_2 semiconductor surface can occur in less than 3 fs. These results directly confirm that electronic coupling of the aromatic molecule to its substrate is sufficiently strong to suppress competing processes[17].

The most efficient photoelectrochemical solar cells are currently based on a nanostructured TiO_2 electrode[3]. The electrode is sensitized to visible light by adsorption of a dye. One of the most promising dyes is "N3"[18] or $(dcb)_2Ru(NCS)_2$ (dcb = 4,4′-dicarboxy-2,2′-bipyridine, also termed bi-isonicotinic acid), which binds to the nanostructured electrode through one[19] or two[1] dcb

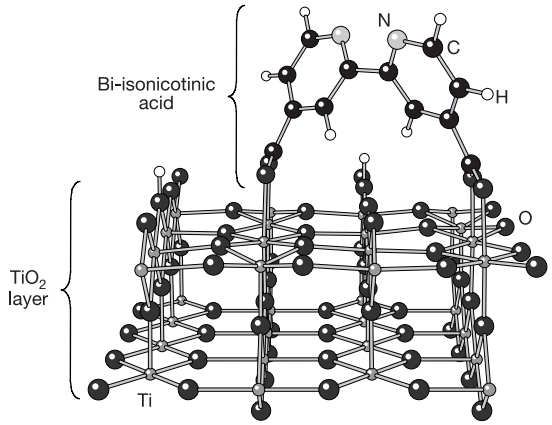

Figure 1 Geometry of the adsorption structure of bi-isonicotinic acid on TiO_2(110). The bonding is on-top for each oxygen atom (2M-bidentate) in both carboxyl groups, with the dissociated hydrogen atoms (small white spheres) assumed to bond to nearby surface oxygen atoms. The pyridine rings are tilted in opposite directions around the inter-ring bond (large white spheres, nitrogen; large black spheres, carbon). The structural model was further refined for the present study using first-principles plane-wave density functional calculations and performing a full optimization of the adsorbate and the surface TiO_2 layer (small white spheres, titanium; large black spheres, oxygen).

ligands. For this dye the above upper limits on the electron transfer time have been measured[5–9]. As a model interface for this important system we have chosen a monolayer of dcb adsorbed on a rutile $TiO_2(110)$ surface[20]. The structure of the interface is illustrated in Fig. 1. The carboxylic groups bind to the substrate in a 2M-bidentate fashion, that is, with each of the carboxylic oxygen atoms attached to one substrate Ti-atom. This geometry is similar to the geometry surmised for bi-isonicotinic acid on anatase $TiO_2(101)$[21] and on anatase TiO_2 nanoparticles grown *in situ* (J.S. *et al.*, manuscript in preparation) as well as to one of two suggested geometries of the original cell[1,19]. The bandgap of rutile TiO_2 (3.05 eV)[22] is close to that of the nanostructured anatase used in the photoelectrochemical cell (3.20 eV)[23]. The high structural quality of a single-crystal surface in ultrahigh vacuum allows a detailed study of the electronic structure of the interface.

The experimental techniques include photoemission spectroscopy (PES), X-ray absorption spectroscopy (XAS), and resonant photoemission spectroscopy (RPES), which are described in the Methods section and in Fig. 2. We employ PES and XAS to assess the electronic density-of-states. RPES probes the interfacial electron transfer dynamics in the low-fs and sub-fs time regimes by monitoring those decay events of the core-excited state that involve the excited electron. A transfer of the excited electron competes with the decay process that in our case takes place on a 6-fs timescale and thus modifies the RPES intensity. The RPES intensities can be compared to the XAS intensities to give electron transfer times (see Methods section for details). In principle, the same information could be derived from a measurement of the XAS lifetime-induced linewidth. However, unresolved vibrational broadening, typical for solid samples, renders such a direct measurement impossible. The periodic pseudopotential calculations provide supporting information about the geometric and electronic structure of the system, and of the interfacial electronic coupling.

The electronic structure of the interface is presented in Fig. 3. The bandgap of the substrate is located between 5 and 8 eV binding energy. We have studied the first three unoccupied states of the adsorbate. The lowest unoccupied molecular orbital (LUMO) is situated almost completely within the bandgap. This is an effect of the core hole (Fig. 2b) produced in XAS, which leads to energy shifts to higher binding energies[24], similar to the case of valence excitations[25]. The other two orbitals (LUMO+1 and LUMO+2), in contrast, lie within the substrate conduction band. The calculations confirm these fundamental experimental results. These findings imply that in the presence of the core hole an electron residing in the LUMO cannot be transferred into the substrate, while for an electron in the LUMO+1 and LUMO+2 a transfer is energetically feasible. We now use RPES to show that the latter cases indeed lead to a very rapid electron delocalization into the substrate.

Figure 4 shows the RPES and contains the XAS from Fig. 3 for comparison. The large peak at 398.6 eV in the RPES shows that the excited electron promoted to the LUMO is localized on the molecule, in agreement with the results for the density-of-states. In contrast, the signals observed in the XAS for the LUMO+1 and LUMO+2 are completely quenched in the RPES, indicating ultrafast delocalization of the excited electron into the substrate. In Fig. 4 we indicate the noise level N of the RPES and the XAS signal intensity S. N is at most 10% of the XAS intensity, that is, $N/S < 0.1$. A possible RPES signal for the LUMO+2 hidden by the noise could thus at most amount to 10% of the XAS intensity S, that is $I_{RPES}/I_{XAS} < 0.1$ in terms of the intensities in the RPES and the XAS. Using the equation given in the Methods section—that is, $\tau_T = \tau_C(I_{RPES}/I_{XAS})/[C - (I_{RPES}/I_{XAS})]$ where $\tau_C = 6$ fs and $C \approx 1/3$ determined from the data in the Supplementary Information—this result corresponds to an upper limit on the electron transfer time, $\tau_T < 2.5$ fs, much faster than previous studies could resolve. For the LUMO+1 the noise level is slightly higher, leading to an upper limit $\tau_T < 3$ fs, which with little loss of precision we adopt for both the LUMO+1 and LUMO+2 states.

This result is semiquantitatively explained by the calculations, which show quite broad LUMO+1 and LUMO+2 bands (compare Fig. 3), with a width of the order of 1.5 eV. Interpreted as bandwidths, and assuming that no vibrational or other broadening effects exist, this corresponds to electron transfer times much shorter than 3 fs. Closer agreement on the resonance energy has been achieved for a simpler system[26], and a similar level of agreement for systems of the present complexity is a challenge for the near future. A key aspect of the present study is that the soft-X-ray excitation frequencies used here are much higher than the fastest possible electron transfer rate. Application of these short electron transfer times to the optical excitations relevant to solar cell applications requires care, because the timescales of both processes are comparable in such cases. Because of this, optical excitation and

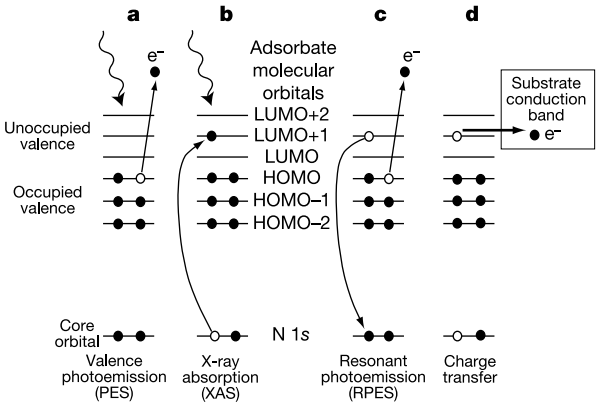

Figure 2 Relevant processes. **a**–**c**, PES, XAS and RPES applied to a molecule. The electronic states are indicated by lines. PES measures the occupied and XAS the local unoccupied density-of-states. RPES monitors the decay of the excited state. **d**, If the molecular orbital couples to the substrate density-of-states an electron transfer may be possible that competes with RPES. HOMO, highest occupied molecular orbital; LUMO, lowest unoccupied molecular orbital. Here, an electron transfer is energetically possible from LUMO+1 and LUMO+2, but not from the LUMO. To the extent that the depicted electron transfer occurs, the RPES is reduced in spectral intensity.

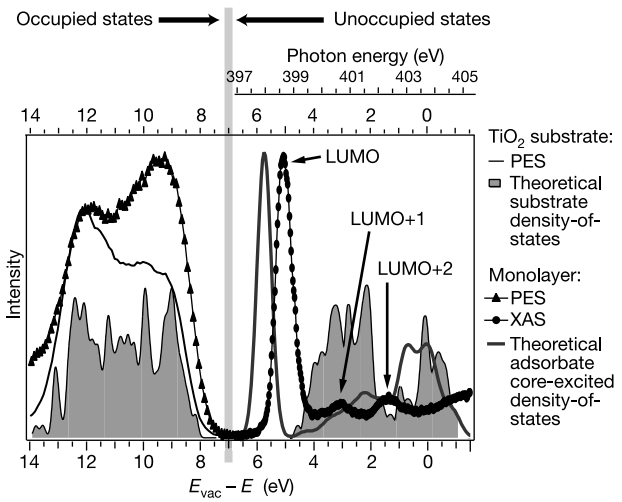

Figure 3 Density-of-states for bi-isonicotinic acid on $TiO_2(110)$: experimental monolayer density-of-states, experimental clean substrate occupied density-of-states, theoretical substrate density-of-states, and XAS calculation. Besides the common energy scale for XAS and PES[16], the photon energy scale for the experimental XAS is given. The LUMO of the excited system lies within the bandgap, but the higher-lying states overlap the conduction band density-of-states. Electronic overlap is necessary for any electron transfer to take place.

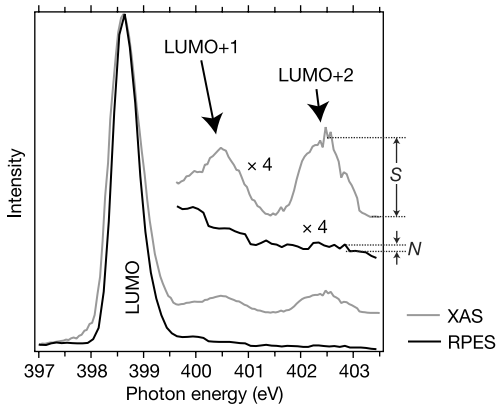

Figure 4 Comparison of RPES and XAS for a bi-isonicotinic acid monolayer. Excitation to the LUMO leads to a large intensity in the RPES owing to strong resonant photoemission, indicating localization of the excited electron on the molecule. For excitation to LUMO+1 and LUMO+2 no RPES-intensity is observed, which implies rapid excited electron delocalization. For the LUMO+1 and LUMO+2, we estimated the maximum possible RPES signal consistent with the noise level *N*, and compared it to the XAS signal *S*, determining the upper limits in the text. The XAS has a 12:1 signal-to-noise ratio at the LUMO+2.

transfer of the electron cannot be disentangled. Hence it is more appropriate to discuss the adsorbate–substrate interaction in terms of coupling strength, that is, in terms of an electron transfer bandwidth (for example, ref. 27), rather than in terms of a well-defined electron transfer time. From the measured electron transfer time of less than 3 fs for a core excitation we can conclude that the system is characterized by strong interfacial electronic coupling. Together with previous calculations[24] the present results show that this extremely rapid transfer relies on the overlap of ring, carboxylic group and substrate electronic states. The weak-coupling Marcus theory commonly used to model electron transfer reactions (for reviews and discussion see, for example, refs 2, 4 and 17) is inappropriate to describe the electronic coupling at these interfaces. This is confirmed by the observation that the electron transfer rate is not limited by the timescale of vibrational motion in this case, although vibrations are excited in the N 1*s* as in optical transitions, here easily observed as the dominant contribution to the width of the LUMO resonance. Similar vibronic coupling is expected for the LUMO+1 and LUMO+2 states. This observation is consistent with at least three models[17,28,29]. Furthermore, the electron transfer takes place on a much faster timescale than charge redistribution[10,11] and thermalization[12–14] in N3 and similar systems.

Aromatic rings such as those in dcb are well known to facilitate charge delocalization. Here we establish that the carboxylic acid group, which forms a covalent bond to the oxide substrate, completes an efficient conduit of electric current from the N atoms into the substrate; the coupling is comparable to the strongest observed for CO on metal surfaces[16]. The large distance introduced by the carboxylic spacer group could be expected to lengthen the electron transfer time[28]. The present results show in contrast that the ligand presents a almost negligible barrier, helping to rationalize the observed ultrafast electron transfer for the N3 dye itself[5–8]. The quantitative application of the present results to the N3 case awaits the ultimate characterization of the N3 bonding geometry. However, the delocalized π-bands will tend to compensate for a single[1] as opposed to a double[19] carboxylate bond, which is also apparent in calculated wavefunctions for the present case[24]. The knowledge gained here should be valuable in strategies for optimizing the charge transfer characteristics of future photovoltaic systems. □

Methods

Photoemission spectroscopy

PES maps the energies of the occupied electronic states of a sample, that is, it images the occupied electronic density-of-states. In the case presented here an electron from an occupied valence state is excited by absorption of a photon with a well-defined photon energy $h\nu$ into the vacuum (Fig. 2a) to kinetic energies E_K of approximately 100 eV. A so-called electron binding energy E_B in the adsorbate–substrate system is derived via $E_B = h\nu - E_K$ and can often be mapped onto electronic density-of-states ground state calculations. Here we call the adsorbate state at lowest binding energy the HOMO (highest occupied molecular orbital), the next one HOMO−1, and so on. The energy scale has its origin at the vacuum level E_{vac} (ref. 16). Clean crystal and monolayer PES spectra were mutually aligned using the O 2*s* level.

X-ray absorption spectroscopy

XAS maps the unoccupied electronic density-of-states. In the present case (Fig. 2b), absorption of a photon with well-defined energy $h\nu$ promotes an N 1*s* core electron to a bound unoccupied state with *p*-character. We term this electron the excited electron. By varying the photon energy different unoccupied states can be reached, and the small spatial extent of the 1*s* orbital ensures that adsorbate states are probed. The first observed state is referred to as the lowest unoccupied molecular orbital (LUMO), followed by the LUMO+1, and so on. The process of removing an electron from a core state, that is, the creation of a core-hole, can quantitatively be viewed as an increase of the positive nuclear charge by one unit[16,26]. Owing to this the observed energies are lower than the calculated ground state energies, especially for the LUMO. The XAS was placed[16] onto the same energy scale as PES.

Density-of-states and XAS calculations

The theoretical curve for the density-of-states is a periodic pseudopotential calculation with gradient corrected functionals of the total ground state density-of-states and was performed using version 3.3 of the CPMD code (for in more detail see http://www.fz-juelich.de/nic-series/Volume3/marx.pdf). It has been aligned to the PES data of clean TiO_2(110), with the gap artificially adjusted to the measured optical one[22]. The XAS has been modelled by calculating the *p*-like density-of-states with an excited N 1*s* electron, which is directly comparable to the experimental data[24].

Resonant photoemission spectroscopy

In XAS the system is left in an excited state with an additional electron in a bound unoccupied level and a vacancy (a missing electron) in a core (N 1*s*) level. This core-excited system will decay exponentially via Auger processes (99.9%), with a time constant given by the core-hole lifetime τ_C (6 fs for N 1*s*). As shown in Fig. 2c, a valence electron (or the excited electron itself) fills the core hole, while another valence electron (or the excited electron) takes up the energy released in that process and is ejected into the vacuum and measured. RPES monitors only decay processes in which the excited electron takes part. These processes are termed resonant photoemission. Because the remaining system is left in the same state as for PES (compare Fig. 2a), RPES measurements are obtained by integrating the valence PES containing the resonant photoemission signal for the photon energies studied in XAS, that is, one probes the effect of placing the excited electron in different unoccupied states. The RPES intensity is then compared to the XAS intensity for each unoccupied state, and results in a particular state-dependent ratio that we call *C* for the case of an isolated molecule (in our case, $C \approx 1/3$, see Supplementary Information). *C* describes the sensitivity of RPES compared to XAS. If the particular unoccupied orbital to which the excited electron was promoted is coupled to unoccupied substrate states, the excited electron delocalizes into the substrate in an exponential process (to first order) with the characteristic electron transfer time τ_T. Thus the transfer process competes with the decay process characterized by τ_C and monitored in RPES (Fig. 2c and d). If the two timescales are comparable the RPES intensity serves as a fingerprint for the extent of excited electron localization. In principle, this enables RPES to probe the electron transfer dynamics within roughly one order of magnitude (up or down) of the core-hole lifetime[15,16]. The transfer time of the excited electron into the substrate can be estimated from the XAS and RPES intensities I_{XAS} and I_{RPES} for the particular unoccupied state from[16] $\tau_T = \tau_C(I_{RPES}/I_{XAS})/[C - (I_{RPES}/I_{XAS})]$. For very fast transfers the RPES vanishes completely for the particular state. This simple model can be applied because the XAS excitation occurs on the 10-attosecond (10^{-17} s) timescale, far shorter than attainable electron transfer times and also far faster than optical excitations. The RPES, the best of several runs, contains a linear, slowly decreasing, direct photoemission background.

Received 11 April 2001; accepted 1 July 2002; doi:10.1038/nature00952.

1. Hagfeldt, A. & Grätzel, M. Molecular photovoltaics. *Acc. Chem. Res.* **33,** 269–277 (2000).
2. Vlček, A. Jr The life and times of excited states of organometallic and coordination compounds. *Coord. Chem. Rev.* **200–202,** 933–977 (2000).
3. Grätzel, M. Photoelectrochemical cells. *Nature* **414,** 338–344 (2001).
4. Miller, R. J. D., McLendon, G. L., Nozik, A. J., Schmickler, W. & Willig, F. *Surface Electron Transfer Processes* (VCH Publishers, New York, 1995).
5. Tachibana, Y., Moser, J. E., Grätzel, M., Klug, D. R. & Durrant, J. R. Subpicosecond interfacial charge separation in dye-sensitized nanocrystalline titanium dioxide films. *J. Phys. Chem.* **100,** 20056–20062 (1996).
6. Hannappel, T., Burfeindt, B., Storck, W. & Willig, F. Measurement of ultrafast photoinduced electron transfer from chemically anchored Ru-dye molecules into empty electronic states in a colloidal anatase TiO_2 film. *J. Phys. Chem. B* **101,** 6799–6802 (1997).
7. Asbury, J. B., Hao, E., Wang, Y., Ghosh, H. N. & Lian, T. Ultrafast electron transfer dynamics from molecular adsorbates to semiconductor nanocrystalline thin films. *J. Phys. Chem. B* **105,** 4545–4557 (2001).
8. Heimer, T. A., Heilweil, E. J., Bignozzi, C. A. & Meyer, G. J. Electron injection, recombination, and halide oxidation dynamics at dye-sensitized metal oxide interfaces. *J. Phys. Chem. A* **104,** 4256–4262 (2000).
9. Benkö, G., Kallioinen, J., Korppi-Tommola, J. E. I., Yartsev, A. P. & Sundström, V. Photoinduced ultrafast dye-to semiconductor electron injection from nonthermalized and thermalized donor states. *J. Am. Chem. Soc.* **124,** 489–493 (2002).
10. Yeh, A. T., Shank, C. V. & McCusker, J. K. Ultrafast electron localization dynamics following photo-induced charge transfer. *Science* **289,** 935–938 (2000).
11. Tachibana, Y., Haque, S. A., Mercer, I. P., Durrant, J. R. & Klug, D. R. Electron injection and recombination in dye sensitized nanocrystalline titanium dioxide films: A comparison of ruthenium bipyridyl and porphyrin sensitizer dyes. *J. Phys. Chem. B* **104,** 1198–1205 (2000).
12. Damrauer, N. H. *et al.* Femtosecond dynamics of excited-state evolution in $[Ru(bpy)_3]^{2+}$. *Science* **275,** 54–57 (1997).
13. Blanchet, V., Zgierski, M. Z., Seideman, T. & Stolow, A. Discerning vibronic molecular dynamics using time-resolved photoelectron spectroscopy. *Nature* **401,** 52–54 (1999).
14. Willig, F., Zimmermann, C., Ramakrishna, S. & Storck, W. Ultrafast dynamics of light-induced electron injection from a molecular donor into the wide conduction band of a semiconductor as acceptor. *Electrochim. Acta* **45,** 4565–4575 (2000).
15. Wurth, W. & Menzel, D. Ultrafast electron dynamics at surfaces probed by resonant Auger spectroscopy. *Chem. Phys.* **251,** 141–149 (2000).
16. Brühwiler, P. A., Karis, O. & Mårtensson, N. Charge transfer dynamics studied using resonant core spectroscopies. *Rev. Mod. Phys.* **74,** 703–740 (2002).
17. Lanzafame, J. M., Palese, S., Wang, D., Miller, R. J. D. & Muenter, A. A. Ultrafast nonlinear optical studies of surface reaction dynamics: Mapping the electron trajectory. *J. Phys. Chem.* **98,** 11020–11033 (1994).
18. Nazeeruddin, M. K. *et al.* Conversion of light to electricity by cis-X_2bis(2,2′-bipyridyl-4,4′-dicarboxylate)ruthenium(II) charge transfer sensitizers (X = Cl^-, Br^-, I^-, CN^-, and SCN^-) on nanocrystalline TiO_2 electrodes. *J. Am. Chem. Soc.* **115,** 6382–6390 (1993).
19. Rensmo, H. *et al.* XPS studies of Ru-polypyridine complexes for solar cell applications. *J. Chem. Phys.* **111,** 2744–2750 (1999).
20. Patthey, L. *et al.* Adsorption of bi-isonicotinic acid on rutile TiO_2(110). *J. Chem. Phys.* **110,** 5913–5918 (1999).
21. Persson, P. & Lunell, S. Binding of bi-isonicotinic acid to anatase TiO_2(101). *Solar Energy Mater. Solar Cells* **63,** 139–148 (2000).
22. Cronemeyer, D. C. Electrical and optical properties of rutile single crystals. *Phys. Rev.* **87,** 876–886 (1952).
23. O'Regan, B. & Grätzel, M. A low-cost, high-efficiency solar cell based on dye-sensitized colloidal TiO_2 films. *Nature* **353,** 737–740 (1991).
24. Persson, P. *et al.* N 1*s* x-ray absorption study of the bonding interaction of bi-isonicotinic acid adsorbed on rutile TiO_2(110). *J. Chem. Phys.* **112,** 3945–3948 (2000).
25. Chang, E. K., Rohlfing, M. & Louie, S. G. Excitons and optical properties of alpha-quartz. *Phys. Rev. Lett.* **85,** 2613–2616 (2000).
26. Sandell, A. *et al.* Bonding of an isolated K atom to a surface: Experiment and theory. *Phys. Rev. Lett.* **78,** 4994–4997 (1997).
27. Lu, H., Prieskorn, J. N. & Hupp, J. T. Fast interfacial electron transfer: Evidence for inverted region kinetic behavior. *J. Am. Chem. Soc.* **115,** 4927–4928 (1993).
28. Ramakrishna, S. & Willig, F. Pump-probe spectroscopy of ultrafast electron injection from the excited state of an anchored chromophere to a semiconductor surface in UHV: A theoretical model. *J. Phys. Chem. B* **104,** 68–77 (2000).
29. Petersson, Å., Ratner, M. & Karlsson, H. O. Injection time in the metal oxide-molecule interface calculated within the tight-binding model. *J. Phys. Chem. B* **104,** 8498–8502 (2000).

Supplementary Information accompanies the paper on *Nature*'s website (http://www.nature.com/nature).

Acknowledgements

We are grateful for financial support to the Consortium on Clusters and Ultrafine Particles and to the ATOMICS Consortium, which are funded by Stiftelsen for Strategisk Forskning, to Göran Gustafssons Stiftelse, and to Vetenskapsrådet. We acknowledge the Swedish National Supercomputer Centre (NSC) for computer time, and the Group for Numerically-intensive Computations of the IBM Research Laboratory Zürich and the Abteilung Parrinello of MPI Stuttgart for help with the calculations.

Competing interests statement

The authors declare that they have no competing financial interests.

Correspondence and requests for materials should be addressed to P.A.B. (e-mail: paul.bruhwiler@fysik.uu.se).

Ecosystem carbon loss with woody plant invasion of grasslands

Robert B. Jackson*, Jay L. Banner†, Esteban G. Jobbágy*, William T. Pockman*‡ & Diana H. Wall§

** Department of Biology and Nicholas School of the Environment and Earth Sciences, Duke University, Durham, North Carolina 27708-0340, USA*
† Department of Geological Sciences, University of Texas at Austin, Austin, Texas 78712, USA
§ Natural Resource Ecology Laboratory, Colorado State University, Fort Collins, Colorado 80523, USA

The invasion of woody vegetation into deserts, grasslands and savannas is generally thought to lead to an increase in the amount of carbon stored in those ecosystems. For this reason, shrub and forest expansion (for example, into grasslands) is also suggested to be a substantial, if uncertain, component of the terrestrial carbon sink[1–14]. Here we investigate woody plant invasion along a precipitation gradient (200 to 1,100 mm yr^{-1}) by comparing carbon and nitrogen budgets and soil $\delta^{13}C$ profiles between six pairs of adjacent grasslands, in which one of each pair was invaded by woody species 30 to 100 years ago. We found a clear negative relationship between precipitation and changes in soil organic carbon and nitrogen content when grasslands were invaded by woody vegetation, with drier sites gaining, and wetter sites losing, soil organic carbon. Losses of soil organic carbon at the wetter sites were substantial enough to offset increases in plant biomass carbon, suggesting that current land-based assessments may overestimate carbon sinks. Assessments relying on carbon stored from woody plant invasions to balance emissions may therefore be incorrect.

One-third to one-half of the Earth's land surface has been transformed by human action[2,4]. Many continuing transformations exchange woody and herbaceous plants[15–18], including deforestation, desertification, and woody plant invasion (the expansion of woody species into grasslands and savannas). Shifting dominance among herbaceous and woody vegetation alters primary production, plant allocation, rooting depth and soil faunal communities, potentially metres underground[15,18], in turn affecting nutrient cycling and carbon storage[19,20]. The two carbon pools most likely to change are woody plant biomass and soil organic matter, the dominant pool of carbon and nitrogen in grasslands[10,20–23]. New woody biomass stores carbon in amounts that depend on the age, productivity and density of the stand. Changes in soil organic carbon (SOC) over the entire rooting zone are much harder to predict, and have the potential to enhance or offset biomass carbon gains, complicating projections of ecosystem carbon storage.

On the basis of a global analysis of more than 2,700 SOC profiles[20], we examined where increased biomass C in woody plants might be offset by SOC losses (see Methods). Across the global data set, the slope of the relationship between SOC and precipitation was 2.6 times higher for grassland vegetation than for shrublands/woodlands ($P = 0.001$; see Supplementary Information). Whereas grassland SOC was statistically indistinguishable from values for woody plants at 200 mm mean annual precipitation, woodlands had 43% less total SOC than grasslands at 1,000 mm ($P < 0.01$). Although suggestive, this analysis lacked a direct test of vegetation change independent of other covarying factors, including soil properties. So we also examined the direct effect of vegetation change at six paired grassland and invaded woody sites along a

‡ Present address: Department of Biology, University of New Mexico, Albuquerque, New Mexico 87131-1091, USA.